Applied Thermal Engineering, Volume 189, May 2021, Article number 116697
DOI:10.1016/j.applthermaleng.2021.116697

# Aerodynamic Limits of Gas Turbine Compressor during High Air Offtakes for Minimum Load Extension

[1] Artur Szymanski [1*]Uyioghosa Igie [1] Kamal Abudu [2]Richard Hamilton
[1]School of Aerospace, Transport and Manufacturing
Cranfield University
Cranfield, Bedfordshire, MK43 0AL
United Kingdom
*Email: u.igie@cranfield.ac.uk

[2]Mitsubishi Hitachi Power Systems Europe
The Point, 37 North Wharf Road
London, W2 1AF
United Kingdom

## Abstract

Renewable energy sources (RES) have become a favoured alternative to fossil fuel energy generation that has been driven by environmental concerns. Their intermittent nature has meant that gas turbines have remained relevant to support them as a backup. Current grid operation requires gas turbines to operate at as low power as possible when their demand drops, and also ramp-up quickly when power generation from renewables declines. Air extraction from a gas turbine compressor can address the first requirement, as this mechanism reduces the load or power of the engine while storing the air for further pressurised reinjection, related to ramp-up rate improvements. This study demonstrates the aerodynamic implications and the limits to air extraction behind the last stage of the compressor, to achieve further minimum load reduction. To achieve this, a zero-dimensional (0D) analytical model of the engine at design and off-design conditions (air extraction) has been used to determine the boundary conditions for a 3D multi-stage compressor Computational Fluid Dynamics (CFD) model. The CFD model shows the aerodynamic implications of low to high air extractions that are limited by choke, high flow separation, and loss in the pressure at the hub region of OGV and last stage stator. As such, the back of the compressor was more affected than the earlier stages. Based on these, the limit of flow extraction is 18% (of the compressor discharge). The compressor of the analytical engine model showed similarity in trends for comparable conditions with the stand-alone 3D compressor, however, more optimistic than the latter. The work has shown that the compressor is capable of high airflow extractions to reduce the minimum load further.

## 1. Introduction

International and local policies propose that industries must reduce their emissions of greenhouse gases. As a result, the European electricity grid is undergoing a shift from the conventional, fossil fuels fired units to renewable energy sources (RES). With a higher priority for RES, gas turbines can be reliable backup units when wind or solar energy supply declines. During the standby mode of the gas



Published by Elsevier. This is the Author Accepted Manuscript issued with: Creative Commons Attribution Non-Commercial No Derivatives License (CC:BY:NC:ND 4.0).
The final published version (version of record) is available online at DOI:10.1016/j.applthermaleng.2021.116697. Please refer to any applicable publisher terms of use.

turbine, it is necessary to operate at fully reduced environmentally compliant power - minimum environmental load (MEL), instead of a complete engine shutdown. One of the key benefits of enhanced MEL, is the reduction in the number of start-ups, potentially extending the life of an engine. Reduction of the load of the engine can be enhanced by pressurised airflow extraction for compressed air energy storage (CAES). The combination of CAES and gas turbine engine can be achieved by extracting a certain percentage of compressed air at the exit of the compressor. Research on air extraction from gas turbines (for energy storage) and approaches for minimum load reduction have been explored in the open literature. These include studies on the effects of combined cycle gas turbine (CCGT) integration with energy storage [1] and a gas turbine coupled with combined cooling, heating and power (CCHP) plant and energy storage [2]. In both cases, the maximum air offtakes or extraction is around 28 – 30%, amounting to a substantial load reduction. Igie et al. [3] studied the effects of air extraction from various compressor locations on an open cycle gas turbine. The work, which focuses on the overall engine performance and limit of extraction, highlights the crucial effects on an engine level. It also indicates that extracting air at the back end of the compressor is the safest, as the inter-stage extraction can push the subsequent stage towards stall. In a similar work on extraction at the end of the compressor, Abudu et al. [4] take this further to include an emissions study. The mentioned investigation shows for the first time, how air extraction can be deployed to achieve lower MEL.

The previously cited studies of engine model analysis are often 0D modelling to prove the concept, lacking further details in the aerodynamic behaviour of the compressor during the extraction process. However, CFD studies often focus on aircraft engines configurations, such as Refs [5] [6] [7] [8] [9]. These works emphasise on the aerodynamic benefits of such an operation (reduced boundary layer and increased efficiency) and stall active control [10]. Air offtakes from transonic NASA Stage 35 of up to 4% of core flow increased the adiabatic efficiency and stall margin by up to 2% and 31% respectively, at various rotational speeds [7]. The CFD study of bleed offtakes on the $6^{th}$ stage of a multistage compressor concerning various extraction rates and locations pointed out that the rotor leading edge is the most favourable, with peak efficiency gains of 0.4% at 5% extraction [11]. Locally aperiodic flow extraction of 5% of core flow rate from the 1.5 stage compressor (IGV+R1+S1) upstream of R1 resulted in strong effects in the tip region of IGV and R1 blades. Additionally, significant flow overturning and reduced entropy generation in the tip annulus area were noticed [12]. The bleeding of air from the compressor of a jet engine, operating at high load, is proven to reduce the adverse effects of secondary flows. These include tip leakage vortex or blockage generation, aligning the vortex trajectory with the flow, thus extending the surge margin [8] [9]. Benefits pointed out in those studies

originate from the passage boundary layer ingestion that contributes to the reduction of losses. As such, local flow extraction of up to 5% is beneficial from an aerodynamic point of view.

With regards to heavy-duty gas turbine engines, the rationale for high air extraction is different. Since they operate at more stable conditions than jet engines, the air offtakes can serve as a method to control the power output. The concept of air extraction from an industrial-scale gas turbine was studied by Cioffi et al. [13]. The work shows the utilisation of the existing single blow-off valve for minimum load extension by air extraction up to 6.5% of the core flow. The outcomes of the analytical and Computational Fluid Dynamics (CFD) study were validated on the power plant, proving the proposed concept. Peltier et al. [14] investigated compressor air offtakes up to 13% from Siemens' F-class engine. High air bleeding indicated loss reduction near the tip region and increased the outlet flow angle by up to 35%, contributing to unwanted flow separation. Leishman et al. [15] experimentally studied cascade stator hub bleed offtakes with large flows up to 15%. They pointed out total pressure losses and flow angle reduction in the hub region and overturning near the tip. Another important aspect is how the extraction is realised. Grimshaw et al. [16] [17] studied the effects of extraction non-uniformity on the flow distortion in a low-speed compressor. With bleed rates up to 6.2%, a substantial distortion in flow distribution at specific configurations may be present – up to 25% of mass flow locally. The velocity field behind the extraction varied circumferentially, causing the upstream stages to deliver non-uniform total pressure; therefore, locally pushing the stage to unstable operation. Cited works did not consider the performance of the whole engine but focused only on aerodynamics.

The approach taken in this study involves the use of 0D analytical engine model and a standalone 3D CFD multistage compressor model. The 3D numerical models provide a superior level of details than lower-dimensional and lower fidelity analytical models. In this case, the 0D model is used to generate design and off-design boundary conditions for the latter, as it is not practical to simulate an engine or even a whole compressor model numerically. The problem under investigation is unusual for the gas turbine in terms of the amount of flow extraction. As such, there are no experimental data to facilitate the specification of boundary conditions for the CFD model. Besides, in practice, data acquisition is not conducted interstage, because of the intrusive nature of the instrumentation. In modelling, there are at least two ways of complimenting the 3D with 0D model interaction. These can be using the 3D high-fidelity CFD model to alter the 0D low-fidelity model as in Refs [18] [19] [20] [21] [22] [23], or vice-versa [24] [25] [26] [27]. In some cases, the process is iterative, where the 3D high-fidelity model updates the performance model, thereby updating the 3D CFD boundary conditions for the next step. The latter is the case in this paper, which is generally referred to as zooming approach in the

mentioned studies. In this study, the 3D model boundary conditions of the compressor are restricted to the values determined by the off-design behaviour of the overall 0D engine model.

The main contribution of this study is in the identification of aerodynamic limits that are related to high offtakes or extraction from the rear of the multistage compressor. The operation is associated with the improvement of the minimum load of a gas turbine and the capacity for energy storage use. The relevant flow phenomenon at these limits is shown and their prevalence for the respective stages. Using an engine model in the absence of experimental data also ensured that indicative boundary conditions reflecting the non-linear turbomachinery matching (between compressor and turbine) were accounted for in the CFD model. Unlike any previous related study, this work brings together stand-alone compressor aerodynamic implications of air extraction with the overall engine power setting.

**Figure 1** is a flow chart that indicates the relations between the 0D model and 3D model. In the first phase, the 0D analytical model is defined, allowing for the first estimation of the air extraction limits. The subsequent phase involves the use of the 0D outputs to define the 3D model inputs, applied both to the design and off-design points. It is an iterative process as some discrepancies between 0D and 3D model can occur, and adjustment of the 0D model is necessary. The 3D multistage compressor is simulated in the third phase, providing new extraction limits, and reflecting the true impact of the air extraction on the compressor behaviour.

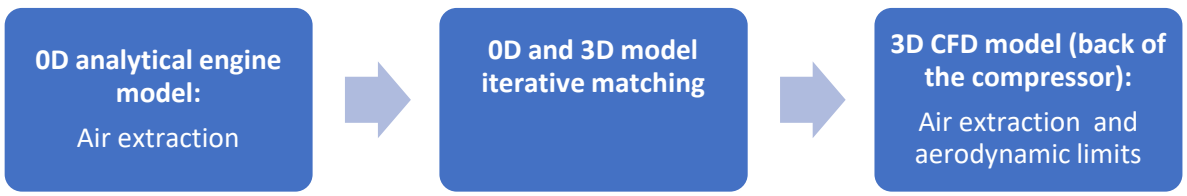



**Figure 1 Flowchart of OD and 3D model processes**

## 2. 0D analytical engine model

The 0D engine model was developed in TURBOMATCH software that is a Cranfield University in-house code, for advanced performance simulation of gas turbine engines. The tool deploys the Newton-Raphson method to solve the non-linearity problem of various rotating components matching. The code uses built-in standard component maps and adjusts them based on required design point input like mass flow, component efficiency, surge margin and pressure ratio. The presented method produces scaled component maps based on scaling formulation that is shown in Refs [28] and [29]. In this study, maps representative of the heavy-duty gas turbine was selected from the embedded library

of compressor and turbine maps. From the compressor point of view, the tool has the capabilities to deploy variable stator angles and performance degradation. Different types of design have been proven to adequately predict various compressor conditions such as fouling [30], degradation [31], washing [32], jet engine cooling [33] and filtration pressure loss effects [34].

## 2.1. Setup and off-design performance

The model deployed in this study is an F-type heavy-duty, single shaft gas turbine engine. The actual engine type consists of sixteen stage compressor and four power turbine stages. The design point parameters of the engine model are presented in **Table 1**, and the layout is shown in **Figure 2**. The compressor was split into four bulk stages, taking into account interstage bleeds for cooling. The division is such that the conditions of comp 4, as shown in the figure, are representative of the overall performance of the 3D CFD model (with 14, 15, 16$^{th}$ and OGV). This ensures that the data from stations 8 and 9 can be inputs to a high-fidelity model. The scheme of the engine cooling flows includes compressor bleeds from interstage stations (4, 5, and 6) and discharge station (9) for turbine cooling, a combustor bypass at station 11 for transition piece cooling, and combustor cooling from station 12 as shown in **Figure 2**.

**Table 1 Engine design point parameters**

| **Intake** | | | |
|---|---|---|---|
| Ambient temperature | 288.15 K | Pressure loss | 1% |
| Ambient pressure | 101325 Pa | Mass flow | 457 kg/s |
| **Compressor** | | | |
| Overall Pressure ratio | 16 | Outlet temperature | 690 K |
| **Combustor** | | | |
| Combustion efficiency | 99.9 % | Fuel flow | 11.0 kg/s |
| Pressure loss | 4 % | Combustor outlet temperature | 1785 K |
| **Turbine** | | | |
| Thermal efficiency | 37 % | Power output | 185 MW |
| Isentropic efficiency | 88.5 % | Exhaust gas temperature | 895 K |

The compressor, combustor and turbine efficiencies, as well as the intake pressure losses, were specified. At the design point, the output parameters are fuel flow, thermal efficiency, and exhaust gas temperature, with the combustor outlet temperature (COT) set as the control constraint. The partially discretised compressor model applied in this study required the specifications of individual lumped stage performance (pressure ratio, isentropic efficiency, and stall margin). The compressor stage-by-stage work coefficient was adopted from published data [35] and general practice for turbomachinery design [36], allowing for the compressor stages pressure ratio and efficiency specification. As for the surge margin, the value of 15% has been applied [37].

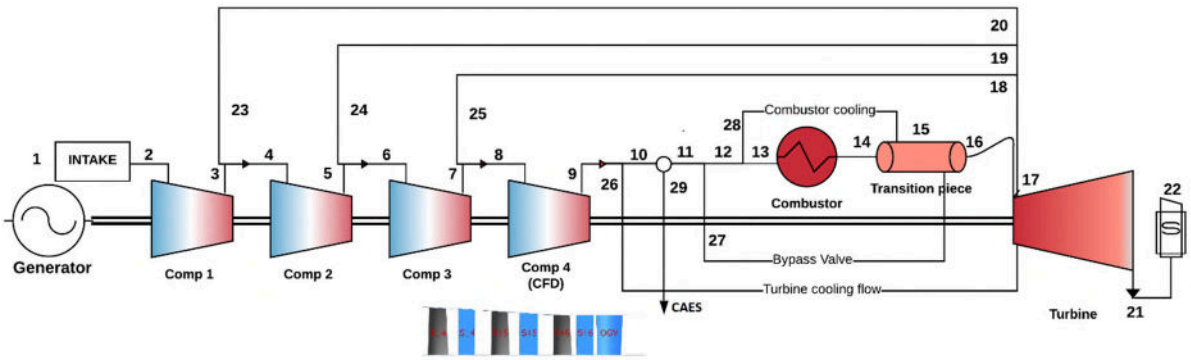
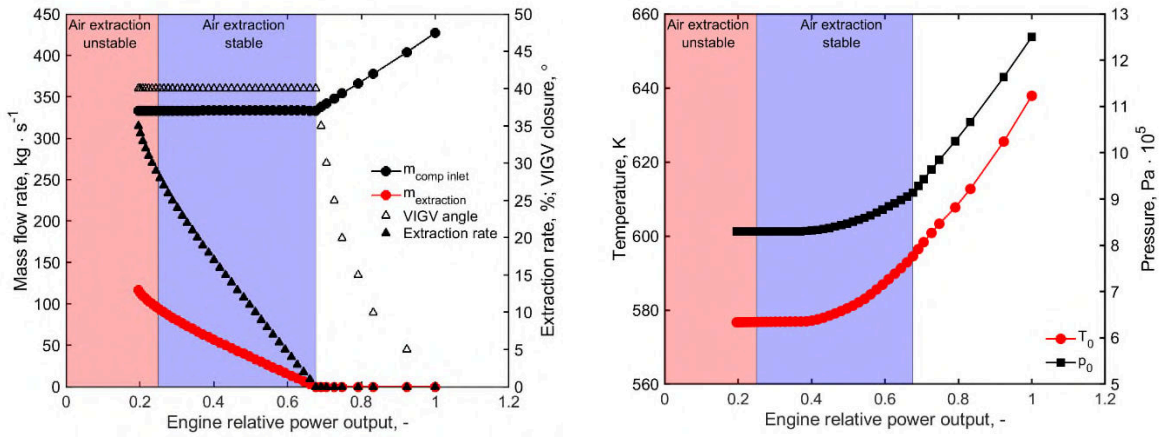



**Figure 2 Layout of engine model indicating the main components and cooling network**

To achieve low loads the Variable Inlet Guide Vane (VIGV) of the engine is closed, followed by the air extraction. These two phases occur with COT kept constant. The closure of the VIGV is deployed by modulating the VIGV angle from 0 to 40°, as shown in **Figure 3a**. The point of 0° is referred to as the maximum opening, while 40° is the maximum closing. The maximum closure of the VIGV reduces the power output to 67.6% of the design value. This point is also the onset of the air extraction that is performed at station 10 (of **Figure 2**). Air extraction turns down the power of the engine further, as shown, to lower power outputs and a region described as unstable. This unstable region (at 30% extraction and above) for the 0D model is related to operations where the extraction pushes comp. 4 towards choke. This is also where the PR of comp. 4 is 1 or lower, where the flow is expected to expand rather than compress. The maximum air extraction of 30% coincides with 24% of power output. **Figure 3b**. shows the corresponding changes in the inlet boundary conditions of comp. 4 during the turndown. These are total temperature and pressure, in addition to the inlet mass flow in **Figure 3a.** The inlet temperature and pressure approached values asymptotic to the x-axis, as extraction increases in the unstable region. More details of this engine turn down operation can be found in Ref [4] that also relates to the emissions.




a) Comp. 4 inlet mass flow and extraction mass flow

b) Comp. 4 inlet temperature and pressure

**Figure 3 Effect of engine turndown on the boundary conditions of comp. 4.**

# 3. 3D CFD Model – Stand Alone Compressor

The CFD model was developed using general-purpose commercial solver Ansys CFX v18.2. The solver uses unstructured element and multiple finite volume method; the variables are defined at mesh elements corner vertices. The discretisation is of second-order with an implicit solution strategy. Ansys Turbogrid was used to generate the structured meshes of the blade channel flow field. The computational setup deployed in the given study assumed high-resolution turbulence numerics and advection scheme. Local calculations of the blend factor were performed, keeping its value close to unity. The working fluid in the simulation is dry air treated as an ideal gas, with variable heat capacity (fourth-order polynomial of temperature). The dynamic viscosity and heat conductivity variation with temperature were represented with Sutherland's formula. The total energy conservation scheme, including the viscous work term, was applied.

## 3.1. Model setup and assumptions

**Figure 4** shows the domain of the CFD model, also highlighting the inlet and outlet parameters (boundary conditions) obtained from the engine model. This figure indicates the last three stages of a multistage compressor with the OGV. The inlet turbulence intensity is set to 5%, which is a recommended value when the exact measurement is unavailable [38]. This value is typical for fully developed flow beyond the middle stages of axial compressors. The mixing stage interface resolves the interaction between rotating and stationary domains. The selected interface ensures realistic steady-state flow averaging and is favoured for single passage multistage turbomachinery simulations. Duct and blade walls were assumed to be smooth and adiabatic. The tip gap of 1% of the blade height is selected for each rotor, while the stator blades were cantilevered with no stator hub leakages.

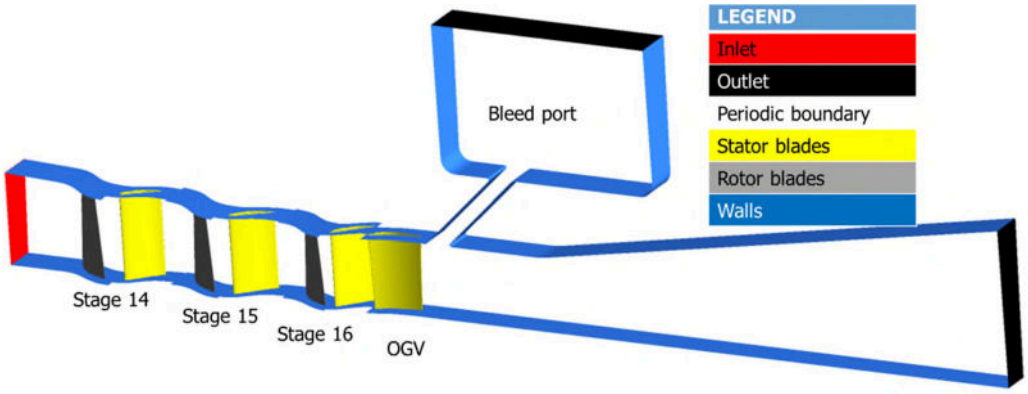



**Figure 4 Multistage CFD model indicating the domains**

For the analysis of the compressor at design condition and extraction operation, some performance indicators have been used as presented in Equations **(1), (2),** and **(3)**. To evaluate them, the values of

pressure and temperature were obtained in between the blades and averaged by local mass flow rate. Since the extraction was performed behind the last compressor stage, no modification to the evaluation of adiabatic efficiency method was considered.

Mass averaged total pressure ratio:

$$\overline{\left({}^{p_2}/_{p_1}\right)} = \frac{\sum_i^{NR}\left(p_{2,i}\cdot \dot{m}_{2,i}\right)/\dot{m}_2}{\sum_i^{NR}\left(p_{1,i}\cdot \dot{m}_{1,i}\right)/\dot{m}_1} \quad \textbf{(1)}$$

Mass averaged total temperature ratio:

$$\overline{\left({}^{T_2}/_{T_1}\right)} = \frac{\sum_i^{NR}\left(T_{2,i}\cdot \dot{m}_{2,i}\right)/\dot{m}_2}{\sum_i^{NR}\left(T_{1,i}\cdot \dot{m}_{1,i}\right)/\dot{m}_1} \quad \textbf{(2)}$$

Adiabatic efficiency:

$$\eta_{ad} = \frac{\overline{\left({}^{p_2}/_{p_1}\right)} - 1}{\overline{\left({}^{T_2}/_{T_1}\right)} - 1} \quad \textbf{(3)}$$

Additionally, the aerodynamic indicators capturing intrinsic local effects were evaluated. The non-dimensional parameters are also useful in the validation and verification of the compressor behaviour at the design and off-design operation. Consistent with accepted turbomachinery aerodynamics principles, they include:

**Diffusion factor (DF)** relating the peak velocity on the suction surface to the velocity at the trailing edge, with one component due to the one-dimensional deceleration of the flow and the second due to the turning of the flow **(4)**. The term related to the turning introduces the blade solidity. A local value DF of 0.6 indicates stall, while a spanwise average value of 0.5 is an upper limit for good efficiency.

$$DF = 1 - \frac{V_2}{V_1} + \frac{\Delta V_\theta}{2\cdot\sigma\cdot V_1} \quad \textbf{(4)}$$

**Total pressure loss** of stagnation pressure is given as ω. In a rotating 3D model of axial compressor blades, this parameter should not exceed 0.02 – 0.03, depending on incidence angle, Mach and Reynolds numbers **(5)**.

$$\omega = \frac{p_{01} - p_{02}}{p_{01} - p_1} \quad \textbf{(5)}$$

**Axial velocity ratio (6):** the changes in axial velocity across the stage have a direct effect on the thickness of the blade boundary layers. If the ratio is slightly above one, it implies that the flow conditions are correct. However, if the ratio is below unity, it means that conditions are worsened. A typical design choice would be to keep the axial velocity rise at approx. 1-2%.

$$\frac{V_{ax,2}}{V_{ax,1}} \quad \textbf{(6)}$$

The flow coefficient in **Eq. (7)** relates the local axial velocity to local tangential velocity of the blade, indicating the air swirl**:**

$$\phi = \frac{V_{ax}}{U} \quad \textbf{(7)}$$

## 3.2. CFD setup verification

To verify the numerical setup, the mesh and turbulence sensitivity study has been performed using stage 14, as shown in **Figure 5**. Three grid resolutions (fine, medium and coarse) were selected, with details shown in **Table 2**. The RANS closure problem was treated with the two-equation Menter's k-omega SST, SST with Reattachment Modification (SST-RM) and (Re-Normalisation Group) RNG k – epsilon model. The SST-RM was introduced due to the better capability to predict turbulence stresses in separation zones, as RANS simulations typically underpredict this, leading to overly large separation zones. Although the SST model is robust enough to predict the onset of separation accurately, it still requires additional production terms under such conditions. SST-RM is also known to provide enhanced results with coarse meshes, as it is typically less sensitive to the level of discretisation. The K-eps RNG model was considered in this analysis, due to its benefits from the Navier-Stokes equation re-normalisation to account for the effects of smaller scales of motion with enhanced accuracy for swirling flows and low-Reynolds-number effects. This makes it also suitable for various turbomachinery flows. **Figure 6** shows the mesh dependence outcomes for the turbulence models, at varied Corrected Mass Flow (CMF). The variation of these CMF corresponds to the variation of the VIGV from 0° to 40°. This shows that the k-epsilon model is generally mesh-independent with negligible differences between the curves. For the SST and SST-RM models, there is some dependence to the mesh quality; however, with little difference between medium and fine resolutions of up to 0.1%. For the k-epsilon, the formulation does not utilise the well-refined boundary layers since the analytical resolution is not dependent on the mesh size. If the boundary layer is resolved within viscous sublayer ($y^+ < 5$), the use of SST is critical to provide accurate resolution near the walls. Additional cross-check showed that the main flow path meshing resolution (especially blades leading edge) had the most substantial effect on the results, while other regions such as tip gap elements = 10, 20, 30, 40 and walls $y^+$ of 1, 2 or 5, had less impact on the performance. The SST-RM model was adopted for

further study due to improved convergence of the simulations, reduced the computations time and proven robustness in the prediction of unstable compressor operation [39]. The medium-mesh case was selected for the multistage compressor, with a total number of 4.0 million cells.

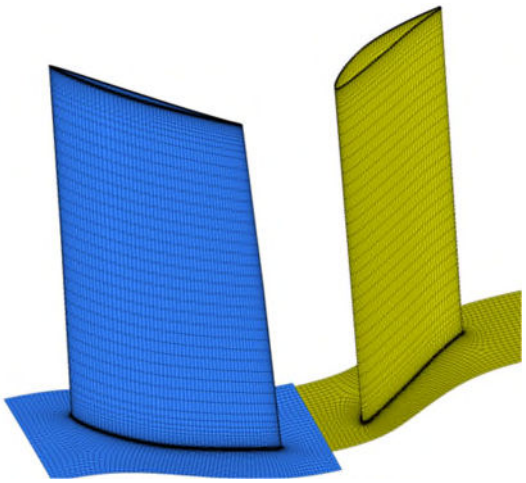
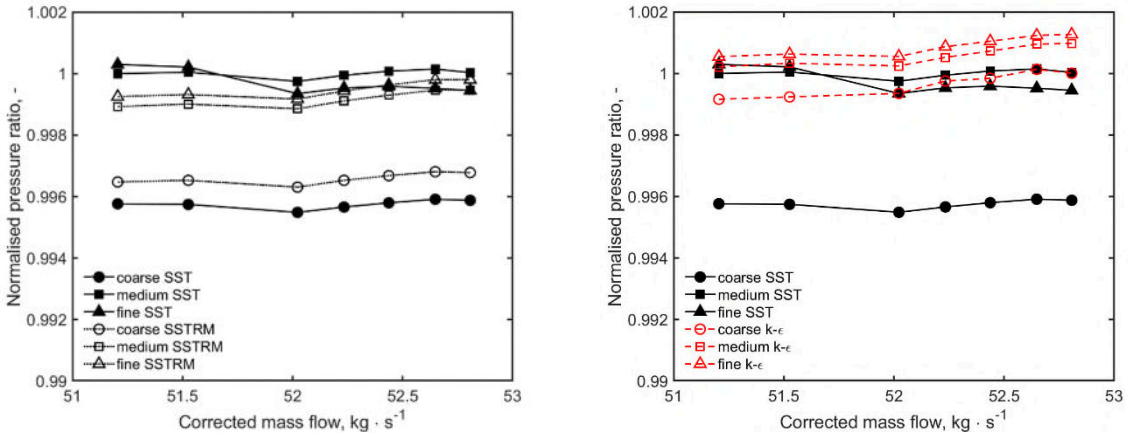


**Figure 5 R14 and S14 blades medium-mesh**

**Table 2 Fine, medium and coarse mesh details.**

| | Fine | | Medium | | Coarse | |
|---|---|---|---|---|---|---|
| | **R14** | **S14** | **R14** | **S14** | **R14** | **S14** |
| **No. of nodes, ax direction** | 84 | 77 | 66 | 60 | 39 | 36 |
| **θ** | 41 | 30 | 32 | 23 | 19 | 14 |
| **r** | 101 | 89 | 78 | 69 | 47 | 41 |
| **Tip gap radial resolution** | 40 | N/A | 30 | N/A | 20 | N/A |
| **Tip gap y+** | 5 | | 5 | | 5 | |
| **y+ blade** | 1 | | 5 | | 5 | |
| **y+ hub** | 2 | | 2 | | 5 | |
| **Total no. of nodes, $10^6$** | 5 | | 2.49 | | 0.32 | |




a) SST and SST-RM b) SST and k-ε

**Figure 6 Influence of turbulence model and number of meshes prediction of pressure ratio**

**Figure 7** shows the aerodynamics indicators evaluated using equations **(4 -(7).** This shows the values obtained for the respective parameters, highlighting that they are within the range for heavy-duty subsonic compressor technology. The figure also shows the variations at different relative power output through VIGV closure, with reference to the engine model. The diffusion factor and total pressure loss are defined in terms of blade-to-blade (rotor and stator separately), while the axial velocity ratio and flow coefficient are defined by stages (rotor and stator together).

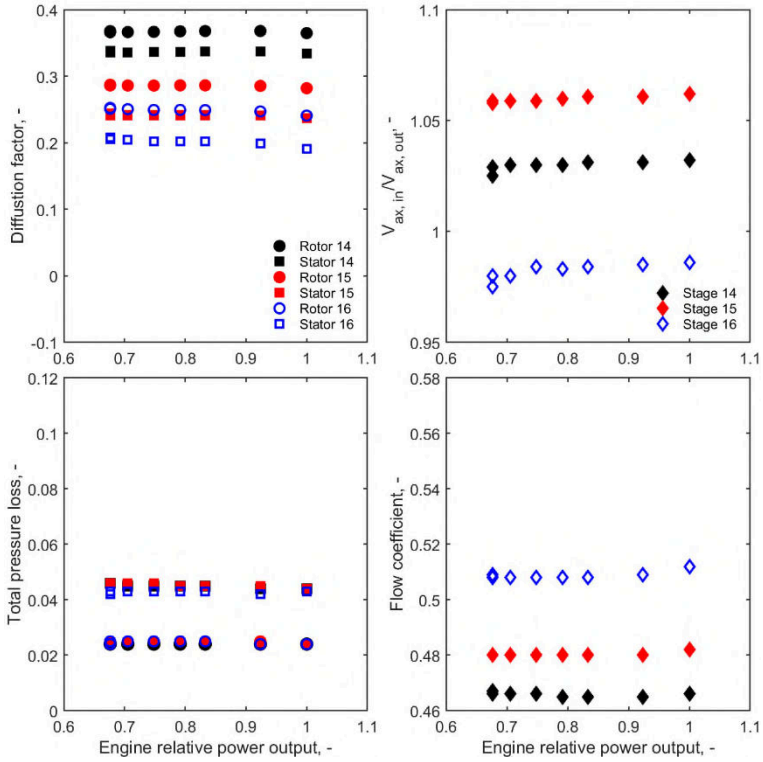



**Figure 7 Verification of aerodynamic indicators of the compressor at different power settings**

## 4. CFD Air Extraction Study

The air extraction is deployed behind the OGV as shown in **Figure 4**. Like the reference case without air extraction, the boundary conditions at the inlet of the domain are obtained from the analytical model. The outlet boundary conditions at the diffuser and bleed port are defined as fixed mass flow rates. The ratio between these mass flows defines the extraction/bleed rate and is known a'priori. Details of the port geometry are presented in **Figure 8.** The design parameters, such as bleed port volume, fillet radii and distance to OGV trailing edge were determined based on existing engines of similar technology, as well as the literature [14] [16]. The permissible range for the extraction port dimensions and adopted values are shown in **Table 3**.

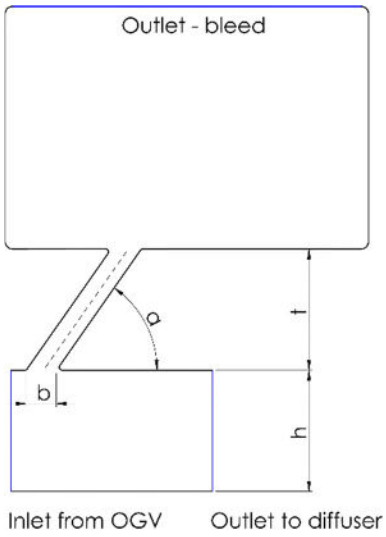



**Figure 8 Extraction port and storage sizing**

**Table 3 Extraction port sizing**

| *Parameter* | *Permissible range* | *Adopted value* |
|---|---|---|
| b/h | 0.25 – 0.35 | 0.25 |
| a | 45 – 135 | 45 |
| t/h | 0.5 – 1 | 0.5 |
| Distance to OGV blade TE | - | 15 mm |

The extraction port was meshed independently from the blades and connected to the OGV outlet and diffuser using General Grid Interface with 1:1 mesh connection. The main path consists of a single blade passage configuration, therefore the bleed port of approx. 2.8° span is modelled with periodic and uniform flow. The mesh sensitivity of the extraction port has been checked, and no modification of results was observed either with halving or doubling the number of cells. The average $y^+$ value of the bleed port walls is evaluated as 9. The resulting total number of grid cells for the multistage case that includes the diffuser and bleed port, was 5.3 million.

## 4.1. Influence of air extraction on compressor performance

The influence of air extraction on the compressor performance: pressure ratio and adiabatic efficiency are presented based on the overall compressor – stages 14 to 16 (the equivalent of comp. 4), as well as the individual stage cases shown subsequently. A variation of the boundary conditions has been considered. This includes the initial case (v) from the engine model, as well as five other cases to gain insight on the sensitivity of the results to the boundary conditions. The range of uncertainty in boundary conditions varied from -1% to 1% for both pressure and temperature, and as shown in **Figure 9**. The range also includes cases where no variation was imposed on at least one of these parameters. The prediction indicates to what extent the air extraction limits are reliable, providing the permissible range as opposed to the absolute value. **Figure 9** shows that increasing the bleed rate from 0% (closed VIGV flow condition) up to 23% generally reduces the pressure ratio and adiabatic efficiency. The pressure ratio reduction occurs due to a loss in total pressure at the OGV, and that of the adiabatic efficiency is attributed to greater loss in pressure ratio than temperature ratio. The results from the 0D analytical engine model can be compared with the CFD predictions. Between 0 – 13% of extraction,

all the CFD results presented lower pressure ratio than the 0D model. For higher rates, only the cases with increased values of boundary conditions predicted higher PR than the 0D input model.

The left-hand side of **Figure 9** also shows that variations in the temperature and pressure have an impact on the prediction and will determine the choke point. For the cases with an increase in temperature and/or pressure, the stability limits are reached at higher extraction rates than the cases of reduced temperature and/or pressure. The stability limits were defined by operating points at which the flow expanded in the compressor, substantial fluctuations in pressure were observed and lacked convergence. The air extraction pushed the compressor towards choke at extraction rates of 12%, 14%, 15%, and 18% for cases ***s***, ***t***, ***u,*** and ***v*** respectively. This also shows that the CFD predictions are more conservative with respect to limits than the case of the engine model. The result of 0D simulations shows an increase in the adiabatic efficiency up to 12.5% of extraction, which was not observed with the 3D model. Like the pressure ratio variations, the trend of adiabatic efficiency from the numerical analysis is seen to overlap the analytical results at high flow rates with increased boundary conditions. The reason for the differences between the 0D and 3D models is a result of different methodology; the 3D model is of high-fidelity, taking into account the aerodynamic losses resulting from the extraction. This includes detailed hub flow separation, stage 16 and OGV blockage generation and elevated total pressure loss shown subsequently. Such a combination of flow phenomenon is unresolved in the 0D model. Hence, this resulted in a delayed choke and therefore, higher acceptable extraction rate. These differences are also reflected in the compressor map of both models shown in **Figure 10** that shows that for the same air extraction rates, the pressure ratio is higher for the 0D model than the 3D case.

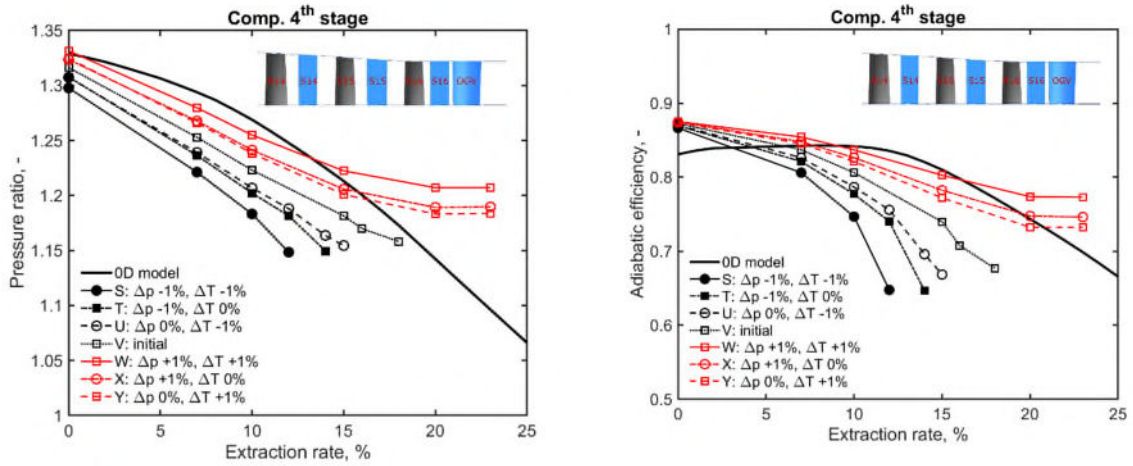



**Figure 9 Effect of extraction on compressor performance: 3D (stages 14 to OGV) and OD (comp. 4) – sensitivity analysis**

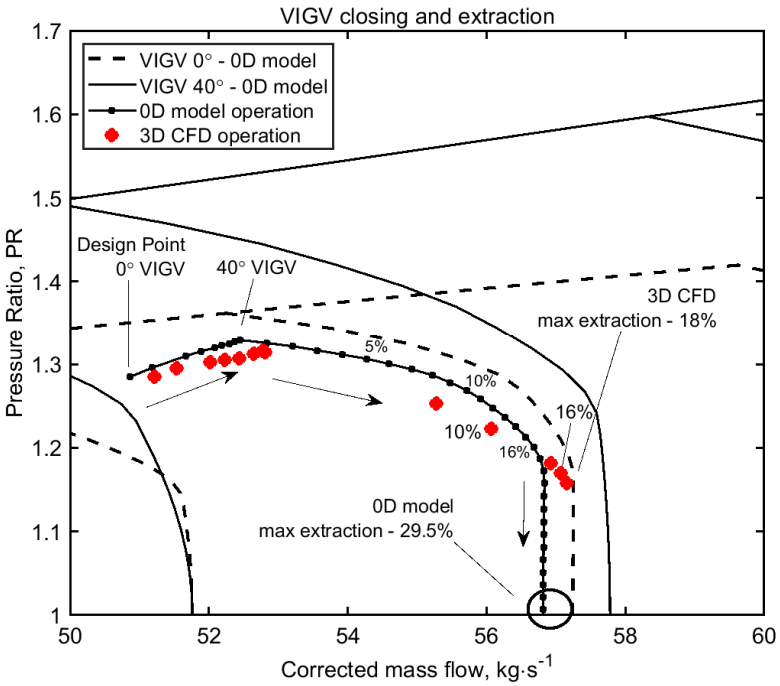



**Figure 10 Compressor maps for the fourth bulk stage – 0D model and 3D CFD**

The stage-by-stage effect of bleeding for the 3D model is shown in **Figure 11**, relevant to the default case v. This shows higher drops in the pressure ratio and adiabatic efficiency with increase in the extraction rate for stage 16 that is attributed to its proximity to the extraction location. Based on the limit related to stage 16, where further bleeding will cause expansion, the maximum air extraction is 18%. At this extraction limit, the reduction in pressure ratios are: 2.4%, 2.8% and 6.2% for stages 14, 15 and 16 respectively.

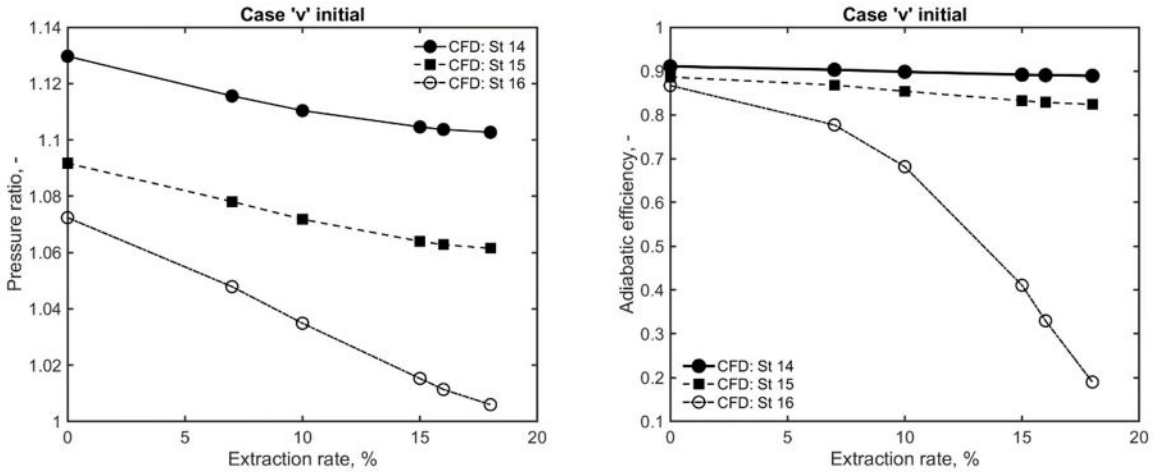



**Figure 11 Stage-by-stage performance of the 3D model for different extraction rate**

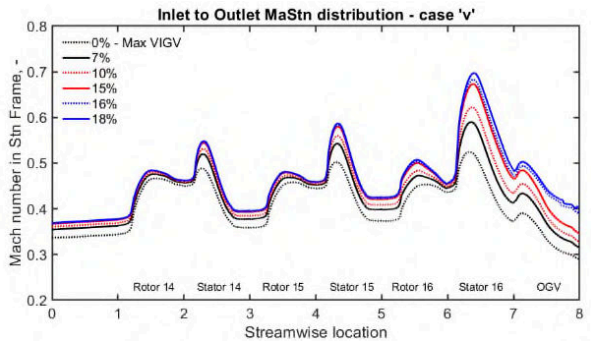
## 4.2. Influence of extraction on the aerodynamic performance

The aerodynamic performance of the 3D model is the focus here, indicating the effects of the bleeding on the respective stages. For a better understanding of flow at the extraction phase, the graphs showing the locally mass-averaged parameters along the axial direction are presented in **Figure 12**. The Mach number (**Figure 12a**) along the compressor increases with the amount of extraction, although not consistently. The highest growth was observed in the stator 16 and the OGV, where the Mach number increased by 38% at the maximum permissible extraction rate of 18%. The increase observed in rotors 14 and 15 is maximum at the rotor inlet (up to 10%) and reduces along the blades. Additionally, a negligible rise is observed between the blades of the rotor and stator.

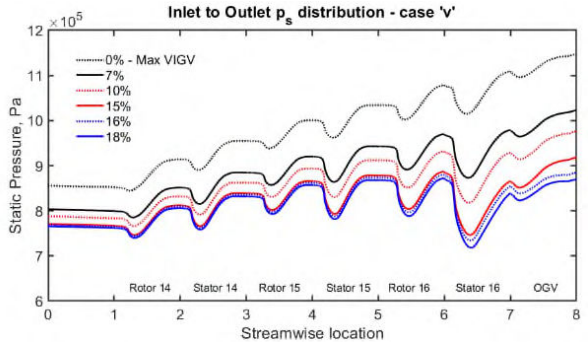
Axial compressors are designed to keep the axial velocity component (**Figure 12c**) constant between the stages, although a slight increase of approx 1% per stage is advised to avoid unfavourable flow conditions. The velocity typically increases in the rotor and stator ducts, and reduces behind the stator to the required values, thus avoiding excessive losses. During air extraction beyond 10%, the axial velocity gradually increases throughout the stages. The front of the compressor is less affected, showing a relatively low acceleration, with the maximum increase of 9.6% observed for rotor 14 in comparison of the default no extraction case. Behind the stator 15, the flow significantly accelerates, due to air expansion. This abnormal behaviour is particularly visible in the stator 16. At the outlet of OGV during high air extraction, the significant disruption of the flow persists as a result of blockage development in the back of the OGV, especially above 15% of extraction rate. The static pressure along the stages (**Figure 12b**) reduces consistently with rising extraction rate. At extraction rates higher than 7%, the static pressure ratio is less than unity over the stator 16, which is an evidence of expansion taking place. Beyond 15% of bleed, the pressure behind the OGV is less than in rotor 16 TE, creating risk for reverse flows.

The velocity flow angle is a crucial factor in the turbomachinery flows, that determines the incidence angles and therefore, the performance and stability. During the air extraction, a strong flow deflection takes place (**Figure 12d**). The rotors outlet angle decreases with air extraction, and each rotating component is affected. The angle reduction is more significant for stages closer to the extraction port as shown. At 18% extraction, the reductions are 2.8%, 3.6% and 6.1% for rotors 14, 15 and 16, respectively. The changes observed from extraction rate 15% to 18% are negligible while cases from 0 to 10% show larger variations. The rotor 16 operates at a much-increased incidence angle and shows signs of abrupt flow overturning at the trailing edge, prior to the stator. The outlet angle is increased by 3° and 7° at 10% and 18% of bleed respectively, directly affecting the efficiency and stator incidence angle. The sudden change of the flow angle contributes to increased aerodynamic losses. Variations

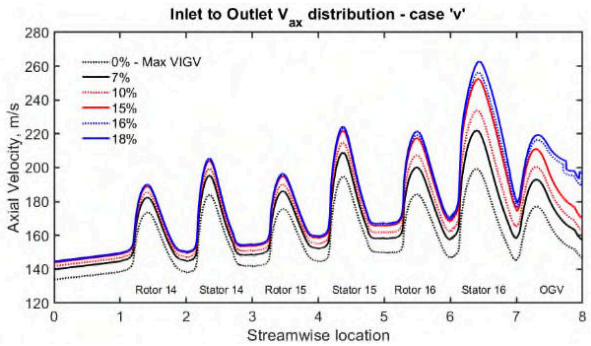
of the flow angle observed in the OGV domain are the result of the blockage occupying a substantial proportion of the OGV duct, thereby pushing the flow towards the casing. The flow angle within stator blades does not change with the elevated flow offtake.



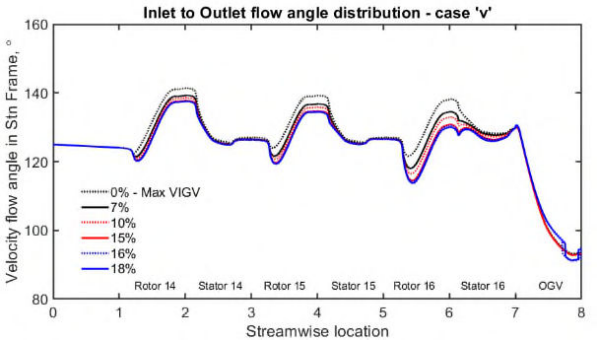

a) Mach number distribution




b) Static pressure distribution




c) Axial velocity distribution




d) Velocity flow angle distribution

**Figure 12 Stage-by-stage axial mass-averaged aerodynamic performance for different extraction rates**

The aerodynamics indicators of compressor stages, during air extraction up to 18% corresponding to relative power output reduction from 67.6% to 38.6% (VIGV fully closed to 18% of air extraction), are presented in **Figure 13**. The air extraction, unlike the VIGV closure shown in **Figure 7**, highly affects all of the indicators. Typically, the diffusion factor reduces with air extraction, while total pressure loss rises. Such behaviour is particularly visible in stage 16, for which conditions are substantially worsened. The diffusion factor drops below zero in stator 16, and the total pressure loss doubles for rotor 16 and triples for stator 16 at maximum extraction, compared to design point operation. Stator 16 located at the back of compressor, closest to the extraction port, is the most affected compressor segment by the off-design operation. Rotor 16 also works under less favourable conditions, although the increase in losses is not as substantial as in the stator. Upstream stages 14 and 15 exhibit an inevitable change in performance, although it is less significant than in stage 16. The flow coefficient and axial velocity ratio increase with air extraction in all of the stages, confirming that the flow

accelerates and straightens out as a result of air expansion. Again, the relative growth of the mentioned parameters is the highest for stage 16.

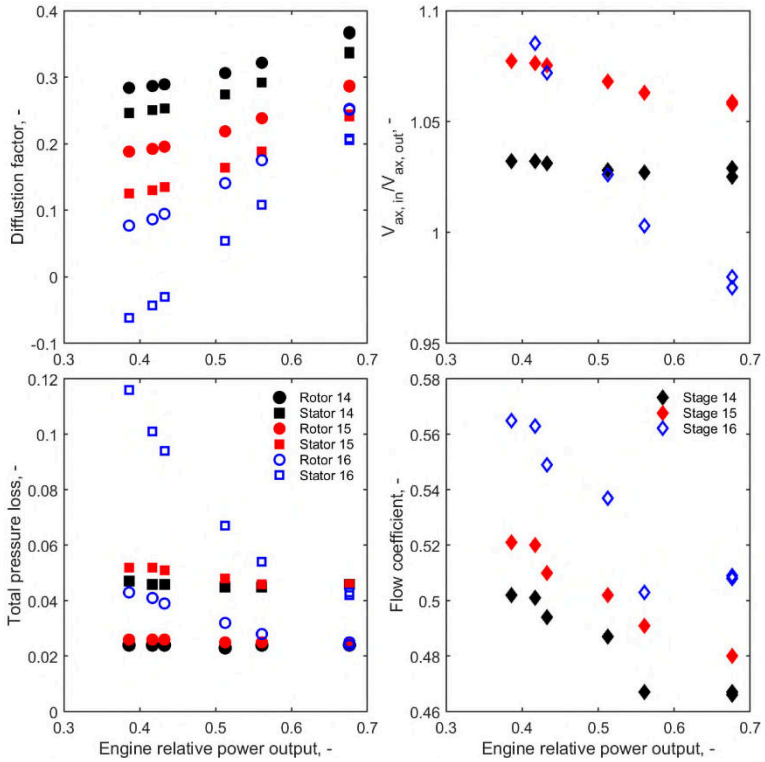



**Figure 13 Aerodynamic indicators of the compressor at air extraction phase**

**Figure 14** presents the spanwise distribution of flow coefficient for selected extraction rate cases. The parameters are pitch-averaged for each blade, behind the trailing edge. At the blade rows from rotor 14 to rotor 16, the flow coefficient increases with the bleed and the changes are consistent along the span. Stator 16 is also shown to be more affected by the bleed, with a higher increase of flow coefficient throughout the span. Radial redistribution at higher bleed rates can be pointed out in the top 15% and bottom 10% of the span. The traverses at the OGV outlet, just downstream of the bleed slot, show a significant change of flow coefficient distribution. At extraction rates of 7-15%, there is an increase of flow function in the tip and hub region. The midspan value is slightly smaller than the peak values in the outer and lower 15% span. However, when the extraction approaches the maximum (16 – 18%) and the compressor is close to choking conditions, substantial redistribution of parameters can be noticed. The peak values of flow coefficient are shifted to the top 10%, and the bottom 35% of span. There is also a considerable deflection near the hub caused by blockage generation in that region.

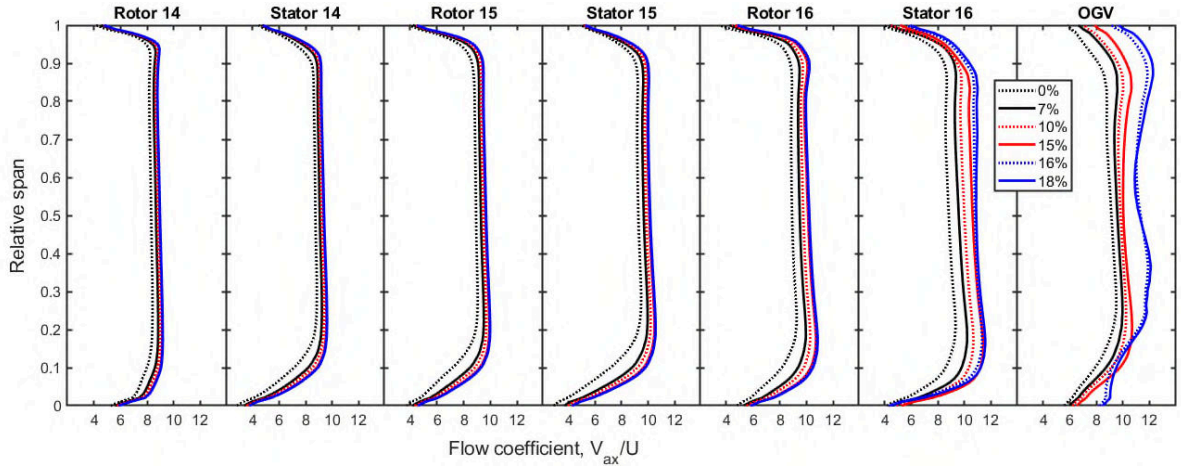



**Figure 14 Stage-by-stage radial pitch-averaged flow coefficient for different extraction rates**

**Figure 15** shows the pitch-wise averaged total pressure loss distribution of the multistage compressor at investigated extraction rates. They present a visible increase in pressure loss as the extraction rate grows. The highest penalty occurs on stage 16, for which the stator is more affected than the rotor. This is further amplified for the OGV. Below 35% of its blade height, the losses created by the corner separation are dominant and contribute to blockage generation. The corner separation is observed even in the case with no extraction, though its magnitude is minute. Negative pressure loss coefficient near the OGV hub is not physical and reflects the reversed flow, characterised by a local pressure ratio lower than unity. The OGV tip and midspan (0.4 to 0.5) pressure losses reduce with extraction, although it is the only region in the entire compressor that benefits from the air extraction. Conversely, these benefits are outweighed by increased losses in other regions of the compressor.

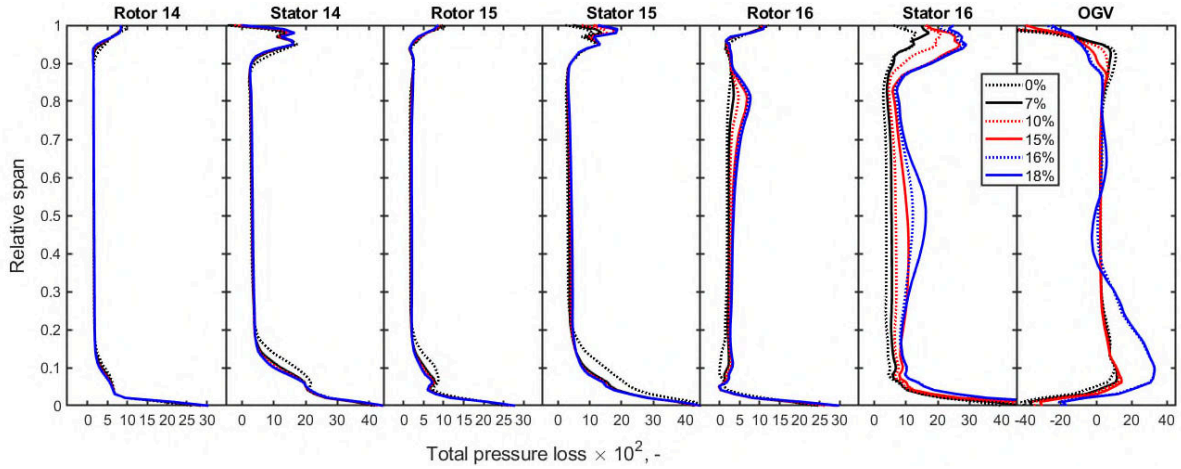



**Figure 15 Inlet to outlet mass-averaged parameters at the range of extractions**

For the Mach number variation, contour plots at different heights across the span (from hub to tip) are presented in **Figure 16**. Only stage 16 and the OGV are considered, given that it has been established that they are the most affected by air bleeding. At 0% extraction condition, the Mach number distribution around the blades is typical for subsonic compressors. The Mach number peaks at 25% to 30% of blades chord on the suction surface of stators and does not exceed 0.6. The typical mid-span Mach number is 0.33, while design principles suggest a range from 0.4 – 0.5.

For the 0% and 10% of extraction, neither separation nor stall is observed between the midspan to the tip of the duct. However, some flow separation was obtained in the near hub region, which is a common and unavoidable effect of corner separation fed by secondary flows on the hub, even without extraction. Regarding the tip region, in the OGV some flow separation at 0% extraction case took place. As well, some flow separation is observed for stator 16 at the intermediate flow extraction of 10%.

For the case of 18% extraction, the OGV tip presents a strong separation between 0-35% of span. The air extraction changes the flow field substantially. Air offtake increases expansion in the stator 16 and OGV, thus reducing the R16 output at the same time. The Mach number is increased in all of the presented regions, contributing to elevated total pressure loss as indicated in **Figure 12a**. The deflection of the rotor angle of stage 16 manifests as flow separation on the pressure side of stator 16 that occupies the substantial area from the mid-span towards the tip. As the bleed port is close to the OGV, the observed wake reduces with growing extraction rate, enhancing the flow conditions in that region. No substantial flow separation is observed within the rotor domain.

The Mach number in the midspan region of the stator radically increases, contributing to adverse flow conditions and loss generation. As the amount of extraction increases, the hub of OGV is being pushed towards blockage condition. The low momentum region in the OGV duct arises from the suction surface and occupies a significant volume. Results for intermediate extraction points were excluded for brevity. In fact, they would present a smoother transition between states of none to maximum extraction. The difference between 15% extraction and 18% (maximum possible) lies in the magnitude of peak values, as the trends show similar regions of high and low energy fluid.

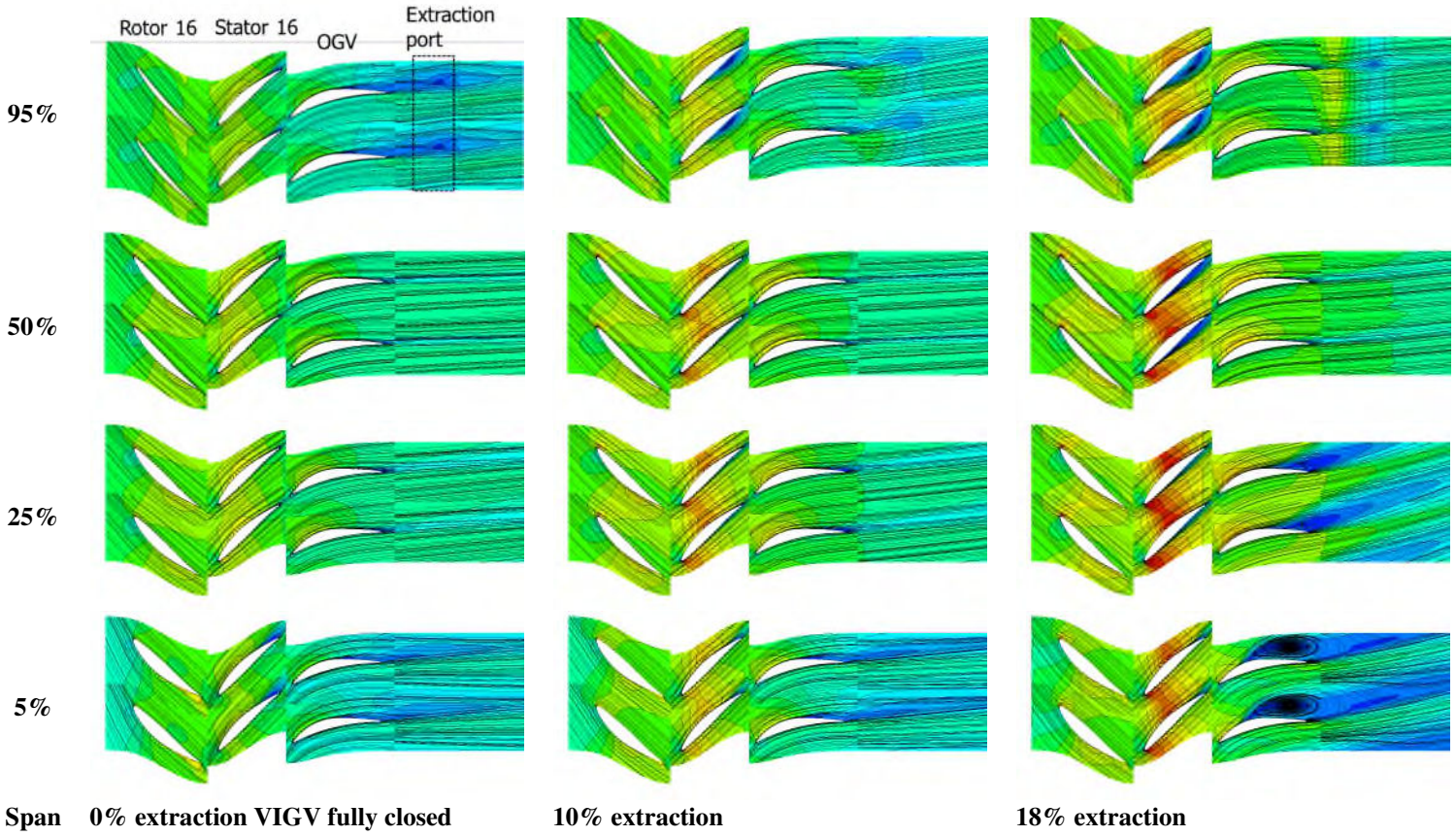
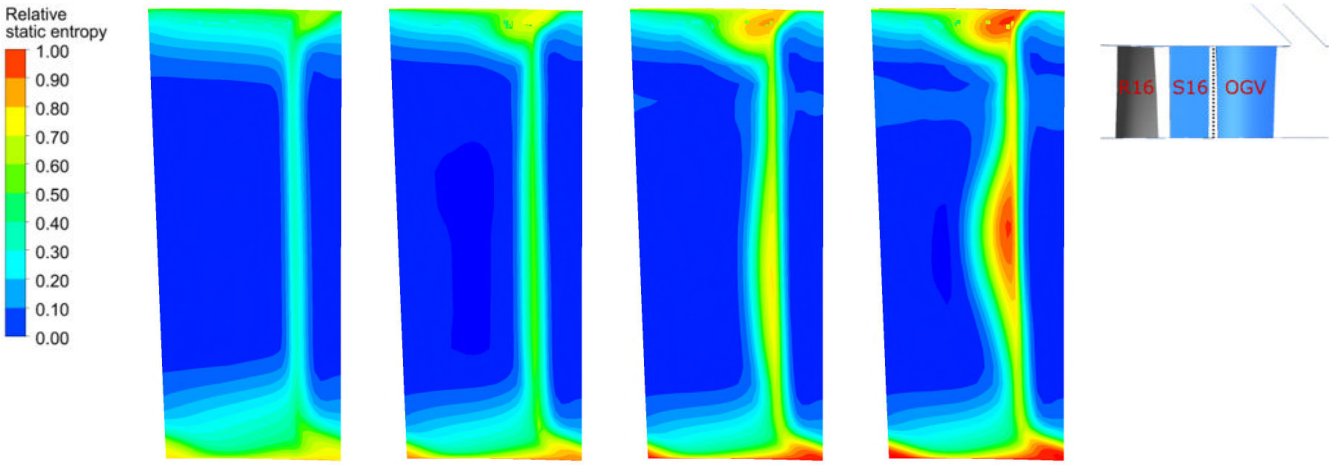



**Figure 16 Contour of Mach number at span locations of stage 16 and OGV for different extraction rate**

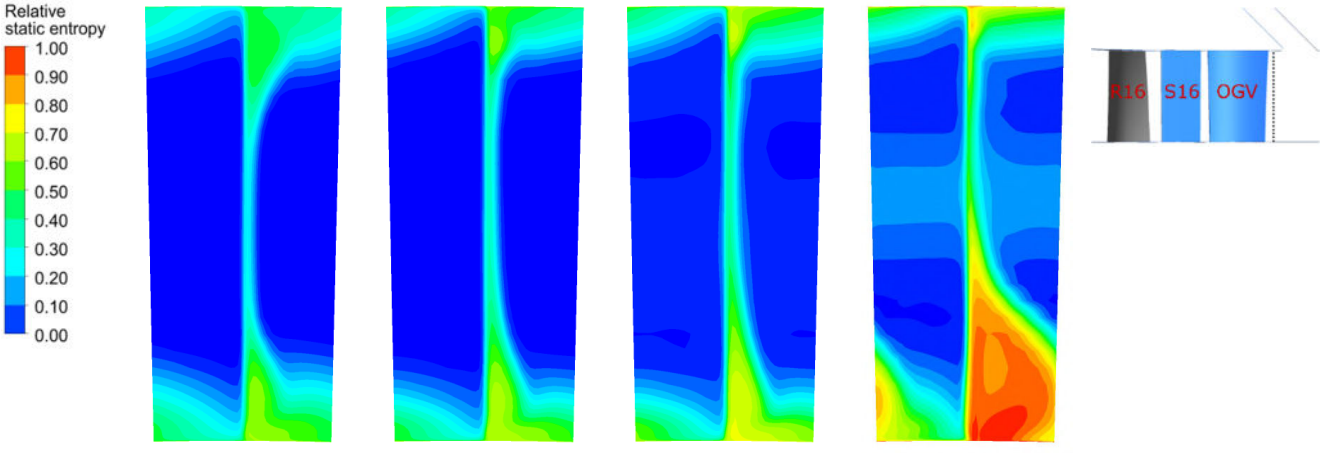
Entropy generation is an indicator of losses present in the flow. It is typically elevated in the proximity to walls (due to the friction between the gas and solid boundaries), mixing and flow separation regions. The contours for static entropy generation behind the stator 16, halfway between S16 and OGV, at various extraction rates are presented in **Figure 17.** With the increase of extraction rate, the hub and tip endwall losses grow. The mid-span region losses increase with air extraction and occupy a larger area of the passage. The thickness of the boundary layer in the tip region remains unchanged, although the losses are more intense. There is no evidence that air extraction would eradicate the shroud boundary layer, as previously observed in Refs [5] [6] [7] [8] [9]. The air extraction increases the diffusion in the hub part of the blade and therefore contributes to escalated blade wake. **Figure 18** shows static entropy generation behind the OGV. Initially, at conditions without air extraction, there are certain losses visible in the casing and hub boundary layer. In the tip region, strong wake persists occupying approx. 10% of the spanwise position. Hub corner stall, near the suction surface, is also present at every operation point, although the magnitude is substantially amplified for the extraction of 15% onwards. When the air extraction is introduced, the shroud boundary layer becomes thinner, and the losses in the tip region reduce, thereby enhancing the tip region flow. Mid-span losses

increase consistently throughout the pitch direction, although the rise is not as significant as in the case of stator 16. The hub losses grew significantly, especially at extraction rates beyond 10% and occupied a large portion of the duct between 0 – 35% of span. Such a substantial increase is caused by blockage and reversed flow behind the OGV. At high extraction rates, air flowing into the bleed port is sucked from the upper part of the channel, creating low energy regions near the suction side of the OGV. High extraction rates of air make the flow conditions through the compressor worse, which is undesirable. A similar phenomenon has been observed experimentally in Leishman [15] with regards compressor air extraction.




0% extraction 10% extraction 15% extraction 18% extraction

**Figure 17 Static entropy contour plots behind Stator 16.**




0% extraction 10% extraction 15% extraction 18% extraction

**Figure 18 Static entropy contour plots behind OGV**

# 5. Conclusions

Analytical and numerical calculations were carried out on a heavy-duty gas turbine engine compressor to explore the effects of high air offtakes to improve engine minimum power setting operations. In the absence of detailed understanding of the aerodynamic behaviour of the compressor in such conditions, a multi-fidelity approach has been taken, for which the 0D analytical engine model has provided the boundary conditions to perform the 3D numerical investigation for the last three stages of a compressor. The study shows that:

- The limits on the maximum air extraction obtained from the 0D model is 30% of the local flow rate. That of the 3D model is more conservative, and between 12 and 18%. Though CFD analysis captures more details (aerodynamics and thermodynamic effects), some of the differences are attributed to the difference in the compressor maps in both cases. The power output at maximum extraction is between 38 – 48% based on the aerodynamics limits in the 3D model, as opposed to 24% in the 0D model that is based only on compressor choke.
- The stage closest to the extraction port is more limited than those in front. The limiting factor is defined by choking which is dominant in the last compressor stator and OGV.
- At high extraction rates, there is a substantial blockage region observed behind the OGV, characterised by reverse flow in the suction side, at the hub.
- Three blade rows upstream of the bleed slot were significantly affected by the air extraction. The local flow disruption was caused by a sudden pressure drop within the compressor and reduced upstream of the compressor.
- No significant benefits of back stage air extraction on stage aerodynamics were observed. The total pressure loss in the tip region of OGV was somewhat reduced but was outweighed by severe hub losses at the same time. The study has made it possible to capture the two mutually exclusive effects: the local reduction of losses due to air extraction and an overall increase in losses that are accompanied in this type of operation. At stages located upstream of OGV (rotor and stator 16, etc.), no flow condition enhancements were noticed.

The work has shown the potential to reduce engine minimum load with air extraction behind the compressor for energy storage. Aerodynamic limits to compressor air extraction are determined by the design of the last stage stator and OGV. An improvement in this area can further extend the extraction quantity; hence a similar effect on the engine load is expected. Though the implications of these off-takes are on the compressor capability, it is crucial to investigate the implications for the combustor in terms of its stability, durability, and emissions. Ongoing studies will attempt to replicate the conditions for critical components.

## 6. Acknowledgement

This study is part of TURBO-REFLEX project that has received funding from the European Union's Horizon 2020 research and innovation programme, under grant agreement No. 764545.

## 7. Nomenclature

| | |
|---|---|
| 0D | 0 dimensional |
| 3D | 3 dimensional |
| CAES | Compressed Air Energy Storage |
| CCGT | Combined Cycle Gas Turbine |
| CCHP | Combined Cooling Heat and Power |
| CFD | Computational Fluid Dynamics |
| CMF | Corrected Mass Flow, kg $s^{-1}$ |
| Comp | Compressor |
| COT | Combustor Outlet Temperature |
| IVG | Inlet Guide Vane |
| MEL | Minimum Environmental Load |
| ML | Minimum Load |
| NASA | National Aeronautics and Space Administration |
| OGV | Outlet Guide Vane |
| PR | Pressure Ratio |
| R | Rotor |
| RES | Renewable Energy Sources |
| RM | Reattachment Modification |
| RNG | Re-Normalisation Group |
| S | Stator |
| SST | Shear Stress Transport |
| TE | Trailing-Edge |
| VIGV | Variable Inlet Guide Vane |

**Symbols**

| | |
|---|---|
| a | Bleed slot inclination angle, deg |
| b | Bleed slot length, m |
| h | Compressor duct height, m |
| m | Mass flow rate, kg $s^{-1}$ |
| p | pressure, Pa |
| T | Temperature, K |
| t | Bleed slot height, m |
| U | Circumferential velocity, m $s^{-1}$ |
| V | Velocity, m $s^{-1}$ |
| y+ | Non-dimensional wall distance, - |

**Subscripts**

| | |
|---|---|
| 0 | Total parameter |
| 1 | Inlet |
| 2 | Outlet |
| AD | Adiabatic (efficiency) |
| ax | Axial component |
| r | Radial component |
| s | Static parameter |

**Greeks**

| | |
|---|---|
| Δ | Difference |
| $\eta$ | Efficiency |
| θ | Tangential component |
| σ | Chord of the blades to their spacing in the peripheral direction |
| ϕ | Flow coefficient, - |
| ω | Total pressure loss, - |

# 8. Reference


[1] Wojcik JD, Wang J. Feasibility study of Combined Cycle Gas Turbine (CCGT) power plant integration with Adiabatic Compressed Air Energy Storage (ACAES). Appl Energy 2018;221:477–89. https://doi.org/10.1016/j.apenergy.2018.03.089.

[2] Yang C, Wang P, Fan K, Ma X. Performance of gas turbine multi generation system regulated with compressor bypass extraction air energy storage. Appl Therm Eng 2020;172:115181. https://doi.org/10.1016/j.applthermaleng.2020.115181.

[3] Igie U, Abbondanza M, Szymański A, Nikolaidis T. Impact of compressed air energy storage demands on gas turbine performance. Proc Inst Mech Eng Part A J Power Energy 2020:095765092090627. https://doi.org/10.1177/0957650920906273.

[4] Abudu K, Igie U, Minervino O, Hamilton R. Gas turbine minimum environmental load extension with compressed air extraction for storage. Appl Therm Eng 2020;180:115869. https://doi.org/10.1016/j.applthermaleng.2020.115869.

[5] Kaluza P, Landgraf C, Schwarz P, Jeschke P, Smythe C. On the Influence of a Hubside Exducer Cavity and Bleed Air in a Close-Coupled Centrifugal Compressor Stage. J Turbomach 2017;139:071011. https://doi.org/10.1115/1.4035606.

[6] Zhao B, Li S, Li Q, Zhou S. Unsteady numerical research into the impact of bleeding on axial compressor performance. Am Soc Mech Eng Fluids Eng Div FEDSM 2010;1:8–15. https://doi.org/10.1115/FEDSM-ICNMM2010-30228.

[7] Cui J, Zhao J, Liu Y, Li S. Numerical research on the safety and performance of transonic compressor with bleed air at multiple operation state. Procedia Eng 2014;80:352–64. https://doi.org/10.1016/j.proeng.2014.09.093.

[8] Gümmer V, Goller M, Swoboda M. Numerical Investigation of End Wall Boundary Layer Removal on Highly Loaded Axial Compressor Blade Rows. J Turbomach 2008;130:011015. https://doi.org/10.1115/1.2749297.

[9] Guinet C, Bettrich V, Gümmer V. Parametric Study of the Bleed Position in a Tip Blowing Casing Treatment. 50th AIAA/ASME/SAE/ASEE Jt Propuls Conf 2014:1–10. https://doi.org/10.2514/6.2014-3441.

[10] Freeman C, Wilson AG, Day IJ, Swinbanks MA. Experiments in Active Control of Stall on an Aeroengine Gas Turbine. J Turbomach 1998;120:637–47. https://doi.org/http://dx.doi.org/10.1016/S0920-5489(99)92014-7.

[11] Wellborn SR, Koiro ML. Bleed flow interactions with an axial-flow compressor powerstream. 38th AIAA/ASME/SAE/ASEE Jt Propuls Conf Exhib 2002:1–10. https://doi.org/10.2514/6.2002-4057.

[12] Gou J, Zhang Y, Su X, Yuan X. Numerical investigation on the effects of real industrial bleeding geometry in a high-speed compressor stage. J Mech Sci Technol 2016;30:5275–86. https://doi.org/10.1007/s12206-016-1046-0.

[13] Cioffi M, Piola S, Puppo E, Silingardi A, Bonzani F. Minimum Environmental Load Reduction in Heavy Duty Gas Turbine by Bleeding Lines. Vol. 3A Coal, Biomass Altern. Fuels; Cycle Innov. Electr. Power; Ind. Cogener., American Society of Mechanical Engineers; 2014, p. 1–11. https://doi.org/10.1115/GT2014-25438.

[14] Peltier V, Dullenkopf K, Bauer H-J. Numerical Investigation of the Aerodynamic Behaviour of a Compressor Bleed-Air System. Vol. 2A Turbomach., American Society of Mechanical Engineers; 2014, p. 1–12. https://doi.org/10.1115/GT2014-25822.

[15] Leishman BA, Cumpsty NA, Denton JD. Effects of bleed rate and endwall location on the aerodynamic behavior of a circular hole bleed off-take. J Turbomach 2007;129:645–58. https://doi.org/10.1115/1.2752191.

[16] Grimshaw SD, Pullan G, Walker T. Bleed-Induced Distortion in Axial Compressors. Proc ASME Turbo Expo 2014 2014;137:1–11. https://doi.org/10.1115/1.4030809.

[17] Grimshaw SD, Pullan G, Hynes TP. Modeling Nonuniform Bleed in Axial Compressors. J Turbomach 2016;138:091010. https://doi.org/10.1115/1.4032845.

[18] Turner MG, Ryder R, Reed JA, Veres JP. Multi-fidelity simulation of a turbofan engine with results zoomed into mini-maps for a Zero-D cycle simulation. Proc ASME Turbo Expo 2004 2004;2:219–30. https://doi.org/10.1115/gt2004-53956.

[19] Pachidis V, Pilidis P, Templalexis I, Barbosa JB, Nantua N. A de-coupled approach to component high-fidelity analysis using computational fluid dynamics. Proc Inst Mech Eng Part G J Aerosp Eng 2007;221:105–13. https://doi.org/10.1243/09544100JAERO37.

[20] Pachidis V, Pilidis P, Guindeuil G, Kalfas A, Templalexis I. A Partially Integrated Approach to Component Zooming Using Computational Fluid Dynamics. Vol. 1 Turbo Expo 2005, ASME; 2005, p. 103–11. https://doi.org/10.1115/GT2005-68457.

[21] Pachidis V, Pilidis P, Talhouarn F, Kalfas A, Templalexis I. A fully integrated approach to component zooming using computational fluid dynamics. J Eng Gas Turbines Power 2006;128:579–84. https://doi.org/10.1115/1.2135815.

[22] Pachidis V, Pilidis P, Texeira J, Templalexis I. A comparison of component zooming simulation strategies using streamline curvature. Proc Inst Mech Eng Part G J Aerosp Eng 2007;221:1–15. https://doi.org/10.1243/09544100JAERO147.

[23] Pilet J, Lecordix JL, Garcia-Rosa N, Barènes R, Lavergne G. Towards a fully coupled component zooming approach in engine performance simulation. Proc ASME Turbo Expo 2011;1:287–99.

https://doi.org/10.1115/GT2011-46320.

[24] Wang ZT, Li J, Li TL, Li SY. Research on Simulink/Fluent Collaborative Simulation Zooming of Marine Gas Turbine. Appl Comput Intell Soft Comput 2017;2017. https://doi.org/10.1155/2017/8324810.

[25] Wang P, Zheng Y, Zou Z, Qi L, Zhou Z. A novel multi-fidelity coupled simulation method for flow systems. Chinese J Aeronaut 2013;26:868–75. https://doi.org/10.1016/j.cja.2013.04.022.

[26] Reitenbach S, Schnös M, Becker R-G, Otten T. Optimization of Compressor Variable Geometry Settings Using Multi-Fidelity Simulation. Vol. 2C Turbomach., American Society of Mechanical Engineers; 2015, p. 1–10. https://doi.org/10.1115/GT2015-42832.

[27] Klein C, Reitenbach S, Schoenweitz D, Wolters F. A fully coupled approach for the integration of 3D-CFD component simulation in overall engine performance analysis. Proc ASME Turbo Expo 2017;1:1–12. https://doi.org/10.1115/GT2017-63591.

[28] MacMillan WL. Development of a modular-type computer program for the calculation of gas turbine off-design performance. Theses 1974 1974;PhD:237.

[29] Pellegrini A, Nikolaidis T, Pachidis V, Köhler S. On the performance simulation of inter-stage turbine reheat. Appl Therm Eng 2017;113:544–53. https://doi.org/10.1016/j.applthermaleng.2016.10.034.

[30] Igie U, Goiricelaya M, Nalianda D, Minervino O. Aero engine compressor fouling effects for short-and long-haul missions. Proc Inst Mech Eng Part G J Aerosp Eng 2015;230:1312–24. https://doi.org/10.1177/0954410015607897.

[31] Igie U, Diez-Gonzalez P, Giraud A, Minervino O. Evaluating Gas Turbine Performance Using Machine-Generated Data: Quantifying Degradation and Impacts of Compressor Washing. J Eng Gas Turbines Power 2016;138:122601. https://doi.org/10.1115/1.4033748.

[32] Igie U, Pilidis P, Fouflias D, Ramsden K, Laskaridis P. Industrial Gas Turbine Performance: Compressor Fouling and On-Line Washing. J Turbomach 2014;136:101001. https://doi.org/10.1115/1.4027747.

[33] Hackney R, Nikolaidis T, Pellegrini A. A method for modelling compressor bleed in gas turbine analysis software. Appl Therm Eng 2020;172:115087. https://doi.org/10.1016/j.applthermaleng.2020.115087.

[34] Igie U, Minervino O. Impact of Inlet Filter Pressure Loss on Single and Two-Spool Gas Turbine Engines for Different Control Modes. J Eng Gas Turbines Power 2014;136:091201. https://doi.org/10.1115/1.4027216.

[35] Smed JP, Pisz FA, Kain JA, Yamaguchi N, Umemura S. 501F compressor development program. Am Soc Mech Eng 1991;1. https://doi.org/10.1115/1.2929140.

[36] Saravanamutto H, Cohen H, Rogers G. Gas Turbine Theory. Fifteenth. Pearsons; 2013.

[37] Walsh P, Fletcher P. Gas Turbine Performance. First Edit. Blackwell Science; 2004.

[38] ANSYS CFX-Solver Modeling Guide, 3. Initial condition modeling; 2020.

[39] Cornelius C, Biesinger T, Galpin P, Braune A. Experimental and Computational Analysis of a Multistage Axial Compressor Including Stall Prediction by Steady and Transient CFD Methods. J Turbomach 2013;136:061013. https://doi.org/10.1115/1.4025583.

DSPACE

https://dspace.org/

# Aerodynamic limits of gas turbine compressor during high air offtakes for minimum load extension

**Szymanski, Artur; Igie, Uyioghosa; Abudu, Kamal; Hamilton, Richard**

**2021-05-05**
Elsevier
https://doi.org/10.1016/j.applthermaleng.2021.116697
Szymanski A, Igie U, Abudu K, Hamilton R. (2021) Aerodynamic limits of gas turbine compressor during high air offtakes for minimum load extension. Applied Thermal Engineering, Volume 189, May 2021, Article number 116697

Downloaded from a DSpace repository. https://dspace.org/